ORIGINAL PAPER

Yam Seep at Four-Way Closure Ridge: a prominent active gas seep system at the accretionary wedge SW offshore Taiwan

Yiting Tseng[1] · Miriam Römer[1] · Saulwood Lin[2] · Thomas Pape[1] · Christian Berndt[3] · Tzu-Ting Chen[2] · Charles K. Paull[4] · David W. Caress[4] · Gerhard Bohrmann[1]

Abstract

Hydroacoustic surveys at the accretionary wedge southwest of Taiwan reveal a confined active hydrocarbon seepage area of ~ 49,000 m^2 in ~ 1350 m water depth on the northern crest of the Four-Way Closure Ridge, which we call Yam Seep. In this study, multibeam and side-scan sonar data acquired during surveys with an autonomous underwater vehicle during an expedition with *R/V Ocean Researcher I* in 2017 showed that the area is characterized by rough topography and high seafloor backscatter. Seafloor observations with a video sled and sediment sampling with gravity corers and the MeBo seafloor drill rig during an expedition with *R/V SONNE* in 2018 revealed that the area is almost entirely covered by intensely fractured methane-derived carbonates, which indicate that seepage has been ongoing for thousands of years. Hydroacoustic anomalies ('flares') in the water column indicated the presence of several gas bubble emission sites mostly at the center and eastern flank of the area in 2019. Drilling through massive carbonates in the northwestern part of Yam Seep induced free gas escape from a depth of ~ 5.1 m. This suggests the presence of gas hydrates in the subsurface as the seep area is located well within the gas hydrate stability zone. The inter-disciplinary investigations of the Yam Seep demonstrate that upward migration of light hydrocarbons and seafloor discharge has a considerable influence on the seabed properties.

Keywords Methane seepage · Authigenic carbonates · Chemosynthetic fauna · Gas hydrate · High-resolution mapping

Introduction

Fluid flow, dewatering, and the ascent of gassy hydrocarbons through ocean sediments are fundamental processes of the Earth's carbon cycle. Such processes not only affect geochemical budgets of the ocean, but migration of fluids and volatiles also plays an essential role in triggering geological processes like submarine landslides, earthquakes, and mud volcanism (Kastner et al. 2014). Subsurface fluid circulation systems can result in focused emission of fluids and/or gaseous compounds from the seafloor into the ocean as cold seeps. These sites are geological windows that can provide important information on the transfer processes and reactions in the geosphere below (Suess 2014). Chemosynthesis-based communities that utilize the chemical energy of reduced compounds such as CH$_4$, H$_2$S and other light hydrocarbons are frequently associated with fluid outflow at seeps (Rubin-Blum et al. 2017; Sahling et al. 2002; Wang et al. 2022). Similar to hot vents, cold seeps support the growth of tubeworms, vesicomyid, and mytilid bivalves, as well as sulfide-oxidizing bacteria (Sibuet and Olu 1998). Biomass production by these communities can be several orders of magnitude higher than typical densities at non-seep environments on the nearby ocean floor (MacAvoy et al. 2002). Authigenic mineral precipitates are further obvious seafloor manifestations of a cold seep. Hydrocarbon-seep deposits are typically dominated by carbonates, but a variety of other precipitates including barite, iron sulfides and gas hydrates are also common (e.g., Bohrmann et al. 1998; Fan et al. 2018;

✉ Gerhard Bohrmann
gbohrmann@marum.de

[1] MARUM-Center for Marine Environmental Sciences and Faculty of Geosciences, University of Bremen, Klagenfurter Str., 28359 Bremen, Germany

[2] Institute of Oceanography, National Taiwan University, Roosevelt Road, 10617 Taipei, Taiwan

[3] GEOMAR Helmholtz-Zentrum for Ocean Research Kiel, Wischhofstr. 1-3, 24148 Kiel, Germany

[4] Monterey Bay Aquarium Research Institute, Moss Landing, CA 95039, USA

Tong et al. 2013; Torres et al. 1996). Mineral authigenesis is linked to biogeochemical cycling of carbon and sulfur (Claypool and Kaplan 1974; Berner and Raiswell 1983; Berner 1990). Carbonate precipitation is induced by the anaerobic oxidation of methane (AOM), and typically occurs at the base of the sulfate reduction zone, which, at methane seeps is often situated close to the seafloor (Paull et al. 1992; Boetius et al. 2000). Due to highly dynamic processes at seeps, the morphology of the seafloor may change during the seepage processes and distinct bottom features are created, like pockmarks, bulges or very irregular surfaces instead of otherwise plain seafloor (Judd and Hovland 2009; Paull et al. 2015).

Cold seeps occur along all continental margins. At active margins, plate convergence and strike-slip faulting are driving tectonic fluid expulsion by dewatering of sediments, which is generating seep fluids from different depths (Scholl and von Huene 2007). Cold seeps at active plate boundaries were reported from the Aleutian Trench (Suess et al. 1998), the Cascadia margin (Suess et al. 1985), Costa Rica (Bohrmann et al. 2002), the Hikurangi margin (Greinert et al. 2010), the Makran Trench (Römer et al. 2012), the Nankai Trough (Sato et al. 2012) and many other oceanic to continental plate convergence zones. Fluid expulsion at passive margins is frequently driven by sediment loading, differences in compaction, saline fluids resulting from contact with evaporitic rocks, and migrating hydrocarbons. These seep sites have been documented along the North Atlantic margins (Paull et al. 1995; Skarke et al. 2014), in the Gulf of Mexico (MacDonald et al. 1990), the Black Sea (Klaucke et al. 2006), the Congo deep-sea fan (Sahling et al. 2008a, b; Pape and Bohrmann 2022), and many other passive margins.

The area studied here is located in the South China Sea. Convergence of the Philippine Sea Plate and the Eurasian Plate formed an active margin in the east and rifting formed the passive margin in the west of the South China Sea (Bowin et al. 1978). Seep research was first focused on the passive margin of the South China Sea, where a Chinese-German research cruise in 2004 discovered seep carbonates exposed in a large area named 'Jiulong methane reef' (Han et al. 2008). Similar methane-derived carbonates, dead and living chemosynthetic bivalves and other seep manifestations were found along the northern and southern continental margins of the South China Sea (Feng et al. 2018b). Detailed investigations using diving platforms like submersibles and ROVs have been performed at active seep sites on Formosa Ridge (Lin et al. 2007; Fujikura et al. 2007; Machiyama et al. 2007) on the northeastern slope and at 'Haima' seep on the southwestern slope of the South China Sea. Both sites are well known for their active gas emissions, methane-derived carbonate precipitates, specific biomarkers, and chemosynthetic bivalves (Feng et al. 2018a; Liang et al. 2017; Wei et al. 2020).

In contrast to the passive margins, seeps along the active margins of the South China Sea are less well investigated although the seafloor sediments and the lowermost water column commonly show elevated concentration of methane (Chen et al. 2017; Chuang et al. 2010, 2013, 2019). Geophysical indications for the widespread presence of gas hydrates also occur within the accretionary prism southwest of Taiwan (Schnürle et al. 2011). Klaucke et al. (2016) investigated seepage at ~ 1500 m below sea level (mbsl) at the so-called Four-Way Closure Ridge (FWCR) by analyzing high-resolution bathymetry, deep-towed side-scan sonar imagery, high-resolution seismic profiling and towed video observations. A prominent seep area identified on top of the northern FWCR is characterized by patches of high seafloor backscatter. Seafloor video observations showed active gas emissions, the presence of extensive authigenic carbonate slabs, and chemosynthetic bivalves (Klaucke et al. 2016).

During a drilling cruise in 2018 using the remotely operated drill rig MARUM-MeBo200 onboard *R/V SONNE* we re-visited the main seep area described by Klaucke et al. (2016). Since the shape of the seep area resembles the root vegetable 'yam', we call the area "Yam Seep". The objective of this work is to constrain the geological processes that have formed the Yam Seep and constrain how they affect seafloor properties and gas seepage. We present new and comprehensive results with a high-resolution video survey from the Yam Seep together with micro-bathymetry data collected with an autonomous underwater vehicle during a previous cruise.

Regional setting

Located at the convergent margin of the Eurasian Plate and the Philippine Sea Plate, southwestern offshore Taiwan is characterized by a deformation front where the South China Sea lithosphere is subducted underneath the Philippine Sea Plate. The Philippine Sea Plate is moving in a northwestern direction against the Eurasian Plate (Fig. 1a) with a convergence rate of ~ 8 cm/year (Ustaszewski et al. 2012). The collision initiated between the middle and late Miocene (Bowin et al. 1978) caused the formation of a series of accretionary ridges and thrust faults. This process created pathways for fluid and gas migration leading to the formation of mud volcanoes and cold seeps at the seafloor (Liu et al. 1997, 2006). The accretionary wedge has been divided into an upper slope and a lower slope (Fig. 1a) (Klaucke et al. 2016; Liu et al. 1997, 2006). The upper slope domain in relatively shallow water hosts a series of mud diapirs, mud volcanoes, and related active gas and mud extrusion (Chen et al. 2014, 2020a, b). The deeper, lower slope domain includes ridges formed by active thrusting and folding and cold seep sites (Chuang et al. 2010, 2013, 2019; Fan et al.
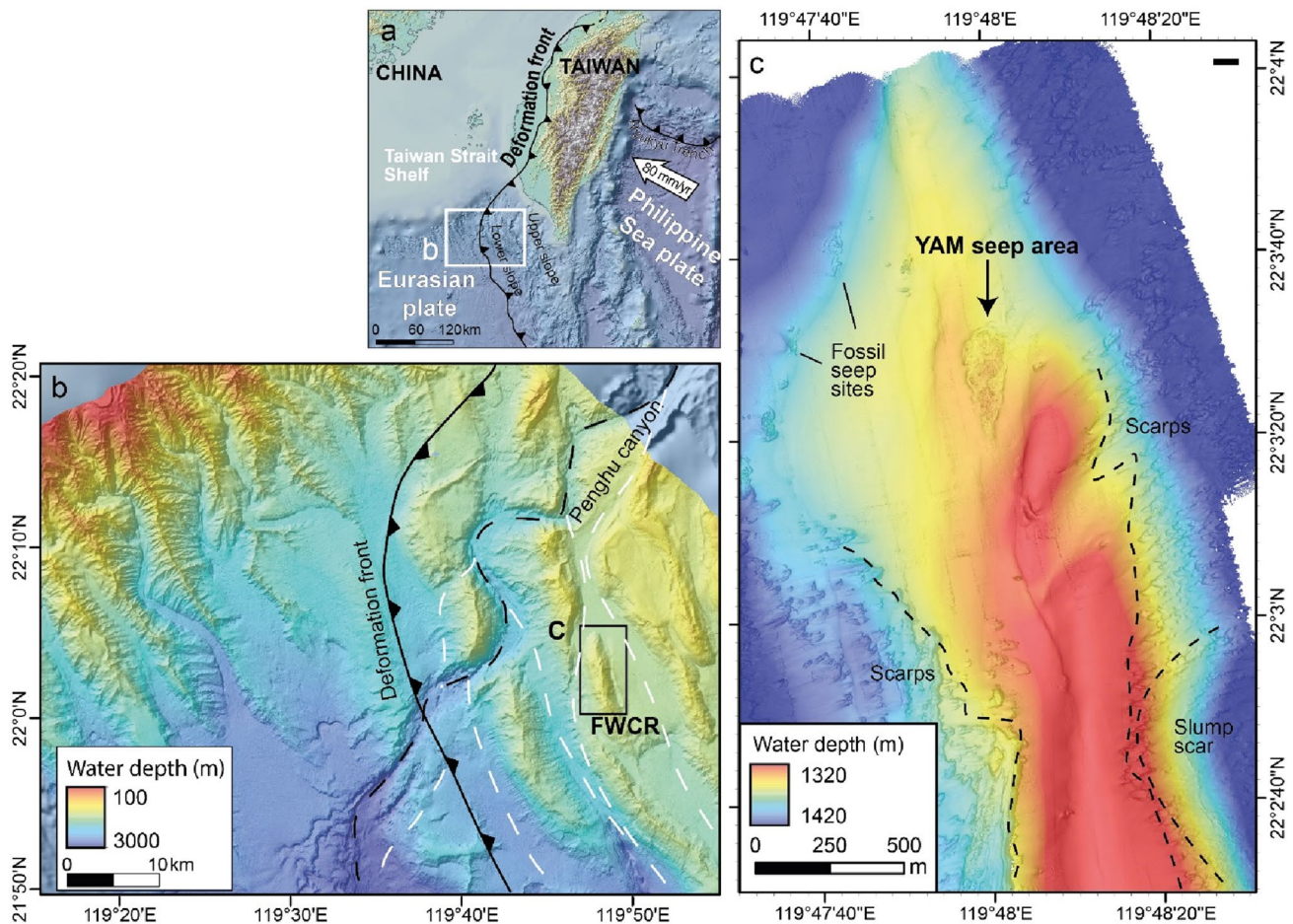
Fig. 1 Tectonic setting of offshore SW Taiwan. **a** Location of accretionary prism SW offshore Taiwan: the deformation front, which is forming the boundary of the Philippine Sea Plate and the Eurasian Plate at the seafloor. **b** Detailed bathymetric map of the transition area from the passive margin in the west to the active margin in the east showing locations of the deformation front (black solid line with arrows) and of NE–SW-trending ridges. Present Penghu canyon is shown with a black dashed line and the former canyons are marked by white dashed lines (Klaucke et al. 2016; Liu et al. 1997; Yu and Chang 2002). **c** 1-m scale bathymetry map based on dives with an autonomous underwater vehicle (AUV) and showing the northern sector of Four-Way Closure Ridge (FWCR) and Yam Seep. Several fossil seep sites, scarps, and slump scars in the area had been reported by Klaucke et al. (2016) and Chen et al. (2020a, b)

2018). Four-Way Closure Ridge (FWCR), which hosts the seep area studied here, is one of the well-developed accretionary ridges (Fig. 1b).

FWCR is a complex anticlinal elongated structure, which is approximately 10 km in length. It is orientated in NNW–SSE direction parallel to the deformation front. It is located at ~ 1500 mbsl and towers up to 350 m above the surrounding seafloor (Fig. 1c). Chen et al. (2020a, b) identified scarps associated with the western and eastern flank of FWCR and Klaucke et al. (2016) suggested the presence of slump scars on its eastern flank (Fig. 1c).

The southwestern Taiwan accretionary prism is characterized by one of the highest weathering rates in the world, and the sediment flux toward SW offshore is estimated to account for 99 Mt/year (Dadson et al. 2003). These sediments are transported into the South China Sea through submarine

canyons, including the Penghu canyon, which controls the erosion of slope sediments along the submarine ridges, and are prominent erosive conduits on the active margin. Penghu canyon (Fig. 1b) was probably once located close to FWCR, as revealed by seismic data showing similarities of deposits at the eastern flank of FWCR, suggesting removal of paleo seafloor (Klaucke et al. 2016; Kunath et al. 2020).

The Yam Seep studied herein is located at the northern crest of FWCR. It is situated on top of an extensional fault network with the main thrust fault structures on its western limb (Kunath et al. 2020). Fluids ascend along the thrust faults and extensional fault systems at shallow depth (Kunath et al. 2020). Bubble emission activity at the seafloor of the Yam Seep has been reported by Klaucke et al. (2016). Mau et al. (2020) reported enrichments of dissolved methane in near-bottom water samples collected in 2018

and showed that the Yam Seep is generally bathed in high salinity deep water. Several fossil seep sites inferred from backscatter anomalies were reported from a close-by area to the northwest of the Yam Seep (Klaucke et al. 2016; Chen et al. 2020a, b) (Fig. 1c).

Materials and methods

This study is based on data obtained during research cruises with *R/V Ocean Researcher I* (ORI-1163) conducted in May 2017 and SO266/1 on *R/V SONNE* conducted in October/November 2018 (Bohrmann et al. 2019). Multibeam bathymetry, seafloor backscatter and side-scan sonar data were also aquired with an autonomous underwater vehicle (AUV) during cruise ORI-1163 in May 2017. Multibeam bathymetry, seafloor and water column backscatter via the ship-borne system, seafloor observation image, sediment cores, and seawater samples were collected during cruise SO266/1. The geo-information system (GIS) software ESRI ArcGIS™ ver. 10.4 was used to create maps and sustainable spatial management of the data obtained during the cruises. The correlated bathymetry and backscatter intensity profiles along the studied track lines were plotted using ArcMap 10.7 3D analyst tool.

Multibeam echosounder data acquisition and processing

A Dorado class AUV developed and operated by the Monterey Bay Aquarium Research Institute (MBARI) (Caress et al. 2008) was used to collect multibeam bathymetry and side-scan sonar backscatter of the FWCR, including the Yam seep area. The AUV was equipped with a Reson 7125 400 kHz multibeam and Edgetech 110 kHz chirp side-scan sonar, both yielding mapping data with a lateral resolution of 1 m. The survey was flown at a 50-m altitude with a 150-m survey line spacing. The AUV survey starting position was initialized using tracking from the GPS navigated ship using an ultra short baseline (USBL) sonar. The realtime survey navigation was derived from a Kearfott inertial navigation system that limits navigation drift to less than 0.05% of distance traveled when aided by velocity estimates from a 300-kHz Doppler velocity log.

Seafloor bathymetry, seafloor and water column backscatter were also obtained using the hull-mounted Kongsberg EM122 multibeam echosounder during cruise SO266/1. The sonar frequency of the EM122 is 12 kHz with an angular coverage sector of up to 150° and 288 beams per ping.

The open source software package MB‑System (vers. 5.5.2213 and 5.5.2289; Caress and Chayes 1996) was used for post-processing of multibeam bathymetry and AUV side-scan data. The AUV navigation was adjusted so that features match in overlapping and crossing swathes using the MB-System tool MBnavadjust. Water column data were displayed and edited to extract hydroacoustic anomalies attributed to rising gas bubbles ('flares') and allowed for manual flare identification and geo-picking of flare sources at the seafloor using the QPS software Fledermaus (vers. 7.7.2) and the FMMidwater tool box. As the seafloor footprint of a flare in the multibeam records was measured at ~50 m in diameter, we define this distance as the approximate error of the geo-picked flare sources. Flare sources identified during different crossings and located within the seafloor footprint were grouped in flare source areas. The 3D projection of extracted anomalies was edited and displayed using the QPS software Fledermaus. The position of AUV multibeam grids was adjusted to fit with the GPS navigated ship-based bathymetry using the Global Mapper® (Blue Marble Geographics) application software. The water column flare data sets and detailed bathymetric data were displayed using the 3D Fledermaus software (QPS).

Coring and drilling

During cruise SO266/1, sediment and carbonate cores were drilled at two sites in the Yam Seep using the seafloor drill rig MARUM-MeBo200 (Table 1, Fig. 2b). Sediment core MeBo-28 (GeoB23234-1) was drilled at the eastern flank of the Yam Seep at 1348 mbsl (Fig. 2b). At this station, a drilling depth of 59.9 m below seafloor (mbsf) with a core recovery of 50.5 m was achieved. Sediment core MeBo-24 (GeoB23225-1) was drilled in the northwestern part of the seep area at 1347 mbsl, down to ~5.1 mbsf. At this station, cemented carbonates were drilled with a core recovery of ~4.9 m and the drilling was aborted when significant amounts of free gas started to escape from the borehole.

Four gravity corer stations were carried out to recover shallow deposits from the Yam Seep and its periphery (Fig. 2b). Two cores, GC-1 and GC-2 (GeoB23203-1 and GeoB23203-2, respectively), were located in the central area of the seep area, whereas cores GC-4 and GC-8 (GeoB23211-1 and GeoB23233-1, respectively) were taken close to its eastern rim (Table 1, Fig. 2b).

Stable carbon isotope analysis of authigenic carbonates

Powdered carbonate sub-samples were reacted to carbon dioxide (CO_2; addition of 100% phosphoric acid at 75 °C) and stable carbon isotope ratios ($^{13}C/^{12}C$ reported as $\delta^{13}C$ in ‰ vs. V-PDB) of the released CO_2 were analyzed with a Finnigan MAT 251 mass spectrometer at the Stable Isotope Laboratory at MARUM. For details of the procedure see Loher et al. (2018).

Table 1 List of gravity coring sites and MeBo drilling sites during cruise SO266/1. GeoB no.: Internal code for stations and samples; n.d.: not determined

Tool	GeoB No./ Station	Water depth (mbsl)	Lat. (N)	Lon. (E)	Approx. sampling depth (mbsf)	Comment
Gravity cores	23203-1/GC-1	1358	22° 03.518'	119° 48.007'	n.d.	No recovery
	23203-2/GC-2	1359	22° 03.521'	119° 48.014'	n.d.	No recovery
	23211-1/GC-4	1354	22° 03.465'	119° 48.036'	5.1	Carbonates at ~4.7 and ~4.8 mbsf
	23233-1/GC-8	1356	22° 03.478'	119° 48.039'	7.2	Carbonates at ~5.1 mbsf
MeBo cores	23225-1/MeBo-24	1352	22° 03.487'	119° 47.979'	5.1	Interrupted due to gas eruption. 4.905 m core recovery; almost entirely carbonate
	23234-1/MeBo-28	1355	22° 03.461'	119° 48.049'	59.9	50.5 m core recovery

Visual seafloor observation

The towed Ocean Floor Observation System (OFOS) on *R/V SONNE* was used for visual seafloor documentation of the Yam Seep during two surveys (OFOS-1 (GeoB23202-1); OFOS-2 (GeoB23206-1); Fig. 2a). The OFOS was equipped with a HD dynamic color video camera (Micro Sea Cam 2002) and a high resolution still frame camera (Canon EOS 5D Mark IV). Positioning of the OFOS was tracked by the IXSEA USBL system. Scale at the seafloor was provided by three laser pointers (Micro-Sea-Laser) of known distance between two laser points (20 cm).

Spatial distribution of dissolved methane in the near-seafloor water body

Four vertical hydrocasts were conducted along a 220 m-long transect across the Yam Seep area on October 20, 2018 (GeoB23208-1, -2, -3, and -4, Table 2). The concentration of dissolved methane in near-bottom waters was previously reported by Mau et al. (2020) in a study of methane over a larger region. In this study, differences in concentrations of dissolved methane are discussed with respect to relative positions above the seep structure.

Results and discussion

Seafloor bathymetry and general composition of deposits

The Yam Seep is located on the summit line of the FWCR at ~1347 mbsl (Figs. 1c and 2a). The seep area is identified as an area with distinctly rougher seafloor, compared with the relatively smooth seafloor in the surrounding area. The seafloor is also characterized by anomalously high seafloor backscatter (Fig. 2b). Together, these seafloor properties characterize a triangular shaped area of ~400 m

maximum length and ~175 m maximum width (Fig. 2b). The total seafloor area characterized by rugged bathymetry is ~49,000 m², whereas the area showing relatively higher seafloor backscatter accounts for ~37,000 m². Both the rough seafloor and high backscatter are considered to reflect seepage-related features, such as high density of authigenic carbonate crusts.

In order to distinguish relative depths within the seep area, a reference plane was created assuming an undisturbed seafloor (Fig. 2a). Elevation difference between this plane and the surveyed seafloor shows two elevated areas as follows: the northern elevated area and the southern elevated area (Fig. 2a). The southern elevated area is an elliptically shaped mound that peaks at a water depth of 1337 mbsl (Fig. 2a). The northern elevated area is characterized by an elongated structure, which reveals two peaks located in its central and western parts. The SW–NE trending topographic profile (profile A1–A2, Fig. 2d) crossing two local elevated areas shows an overall slope gradient of ~2.8° and a total water depth variation of 19 m.

The seep area shows an inhomogeneous, reticular appearing backscatter pattern, which is mainly N–S to NW–SE directed. Highest backscatter intensities were found along the rim of the seep area, with the largest high-backscatter area at the western rim (Fig. 2b). N–S-oriented high backscatter branch-like patterns correlate well with the location of seafloor fractures illustrated in the micro-bathymetry map (Fig. 2a and b). Three separate high seafloor backscatter patches of ~7 m in diameter were identified within circular seafloor depressions a few meters to the west and south of the main seep structure (Fig. 2a and b).

The failure of two gravity corer deployments (GC-1 and GC-2) to recover sediments (Figs. 2a and 3) are assumed to result from the presence of carbonates in near-surface sediments, which prevented penetration. Visual inspection during landing of the MeBo system at station MeBo-24 showed a flat sediment covered surface. Drilling at this station had to be aborted at a coring depth of ~5.1 mbsl (Fig. 3), because
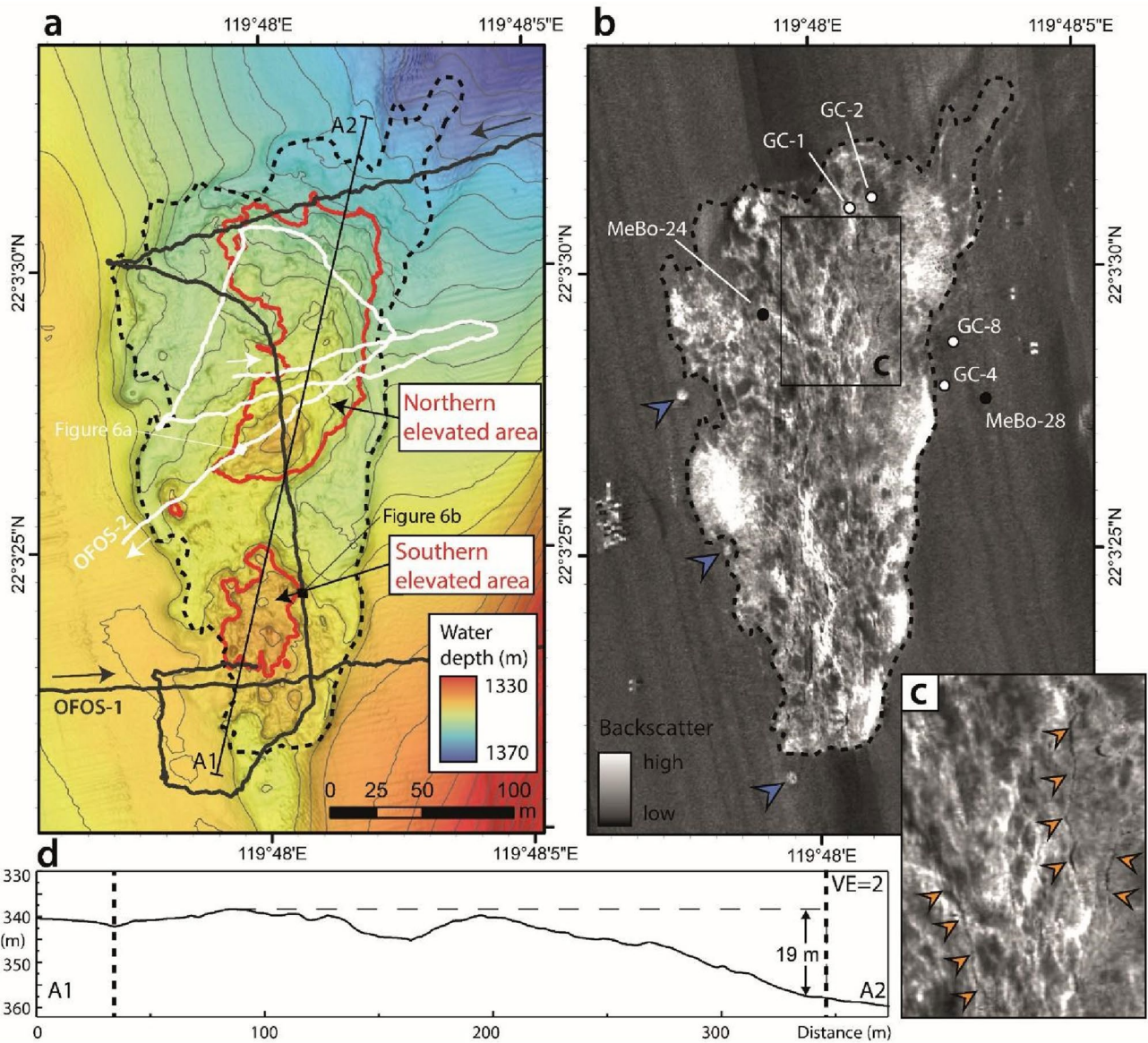
Fig. 2 **a** AUV-based micro-bathymetry of the Yam Seep with tracks of the two OFOS deployments. Black dashed line outlines the area of relatively high backscatter, i.e. the main seep structure (adopted from **b**. Red lines outline relatively elevated areas. **b** AUV-based seafloor backscatter map of Yam Seep illustrating relatively higher backscatter values in contrast to homogeneous, low seafloor backscatter in the surrounding. Blue arrows indicate separate, small sized high-backscatter patches outside the perimeter of the main seep area. White and black dots indicate locations of gravity cores (GC) and MeBo drill sites. **c** AUV-based seafloor backscatter map outlined in **b** with the lighter color being higher backscatter. Orange arrows mark pronounced linear features. **d** Topographic profile 'A1–A2' (location depicted in **a**) indicating a general incline of the seafloor towards northeast with a slope angle of ~2.8°. Dashed line indicates the highest elevation along the profile, which is about 19 m lower at A2

Table 2 List of water sampling stations and water depths. GeoB no.: Internal code for stations and samples

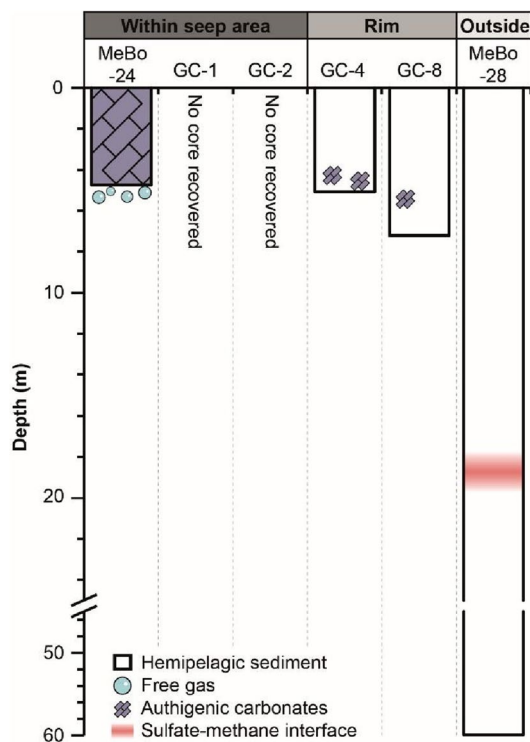| GeoB no.	Station	Water depth (mbsl)	Lat (N)	Lon (E)	Sampled water depth (mbsl)
23208-1	CTD-2-1	1349	22° 03.428'	119°47.963'	1339, 1334, 1329, 1324, 1319
23208-2	CTD-2-2	1347	22° 03.461'	119° 48.000'	1337, 1332, 1327, 1322, 1317, 1311
23208-3	CTD-2-3	1355	22° 03.471'	119° 48.039'	1345, 1340, 1334, 1329, 1325, 1320
23208-4	CTD-2-4	1357	22° 03.479'	119° 48.064'	1347, 1342, 1337, 1333, 1327, 1322

Fig. 3 Schematic descriptions of MeBo and gravity cores (GC) taken within, at the rim, and outside the Yam Seep. See Fig. 2b for core locations

of virulent escape of bubble-forming gas that apparently was ascending from below this depth. Core MeBo-24 revealed about 4.9 m of carbonates consisting of whitish botryoidal and acicular aragonite, grayish micrite, and cemented shells, which likely have sealed the pathway to rising free gas from the deeper accretionary structure. Stable carbon isotope signatures of the carbonates ($\delta^{13}C$-$CaCO_3$) ranging from -37.9 to $-58.3‰$ V-PDB suggest that they represent methane-derived authigenic carbonates (Naehr et al. 2007) with the carbon incorporated primarily originating from the AOM.

Hemipelagic sediments were recovered at stations GC-4 and GC-8 close to the eastern rim of the Yam Seep and at station MeBo-28 further east of the seep area (see Fig. 2b for locations). Concentrations of sulfate dissolved in pore waters extracted from these cores showed only slight depletions with depth (Bohrmann et al. 2019). This indicates that the zone of the sulfate–methane-interface (SMI) was situated well below 4.8 mbsf (GC-4) and 6.9 mbsf (GC-8), respectively. These cores penetrated into the sediment and indicate that upward flux of methane is low at these sites at present (see, e.g., Borowski et al. 1996). Core MeBo-28 was located further east of the seep area (Fig. 2b) and recovered sediments down to 59.8 mbsf. The pore water sulfate concentrations indicate a modern SMI located at ~14–20 mbsf (Bohrmann et al. 2019; Fig. 3). Carbonate precipitates were

present at ~4.7 m and ~4.8 mbsf depth in core GC-4, and at ~5.1 mbsf in core GC-8 (Fig. 3).

Spatial distribution of seepage sites and temporal variability of gas ebullition

During cruise SO266/1 in October 2018, hydroacoustic anomalies in the water column indicative of gas bubble emissions, called flares, were recorded during eight crossings of the Yam Seep. Vertical seafloor projections of the flares, called flare source points, suggested seafloor gas emissions from 41 seafloor sources (Fig. 4b). However, due to echosounder footprint and the corresponding uncertainties of the flare source point locations, we postulate a minimum of eight flare source areas (Fig. 4a) including repeated sightings of flares from the same source areas. Flare source points assigned in 2018 were mainly concentrated along the northeastern rim and the center of the seep area. Such flares could be traced from the seafloor to about 880 m above seafloor (i.e., 550 mbsl) (Fig. 4c). The AUV side-scan survey conducted in spring 2017 revealed the presence of two bubble emission sites located at the northern center of the seep area (Fig. 4a). While one site was located inside the flare source area interpreted from the ship-based flare detection in 2018, no gas emission was observed for the other site in 2018.

3D flare extractions enabled characterization of the variation of bubble emission sites, bubble rise, and intensity. Multiple flares were sometimes observed to occur simultaneously, with three simultaneous flares on 10/20/2018 with maximum heights of 550 m (Fig. 4b). The highest single flare observed during a crossing on 10/31/2018 reached a height of ~880 m above seafloor (Fig. 4c). These results indicate that while gas bubble seepage has persisted for at least several years within the Yam Seep, the particular venting sites varied spatially and temporally. Our flare analysis revealed that gas bubble emission in 2018 was sourced from at least eight areas along the northeastern rim and from central areas of the Yam Seep. However, the bubble ebullition was spatially and temporally variable during different years and even different days of observation.

The variations in the dissolved methane concentrations in discrete water samples collected over the Yam Seep in 2018 (Mau et al. 2020) match results from hydroacoustic investigations. Maximum concentrations of dissolved methane (18.2 nmol/L) were measured in a water sample collected ~5 m above seafloor (1399 mbsl) at the western rim of the seep area during station CTD-2-1 (Fig. 5). Elevated methane concentrations of up to 10.3 nmol/L were also measured in samples taken at the eastern rim of the seep area at ~5 and 10 m above seafloor (1340–1345 mbsl) during CTD-2-3. Concentrations of dissolved methane in samples from above the central seep area (cast CTD-2-2) ranged between ~5.5 and ~6.4 nmol/L, with highest relative

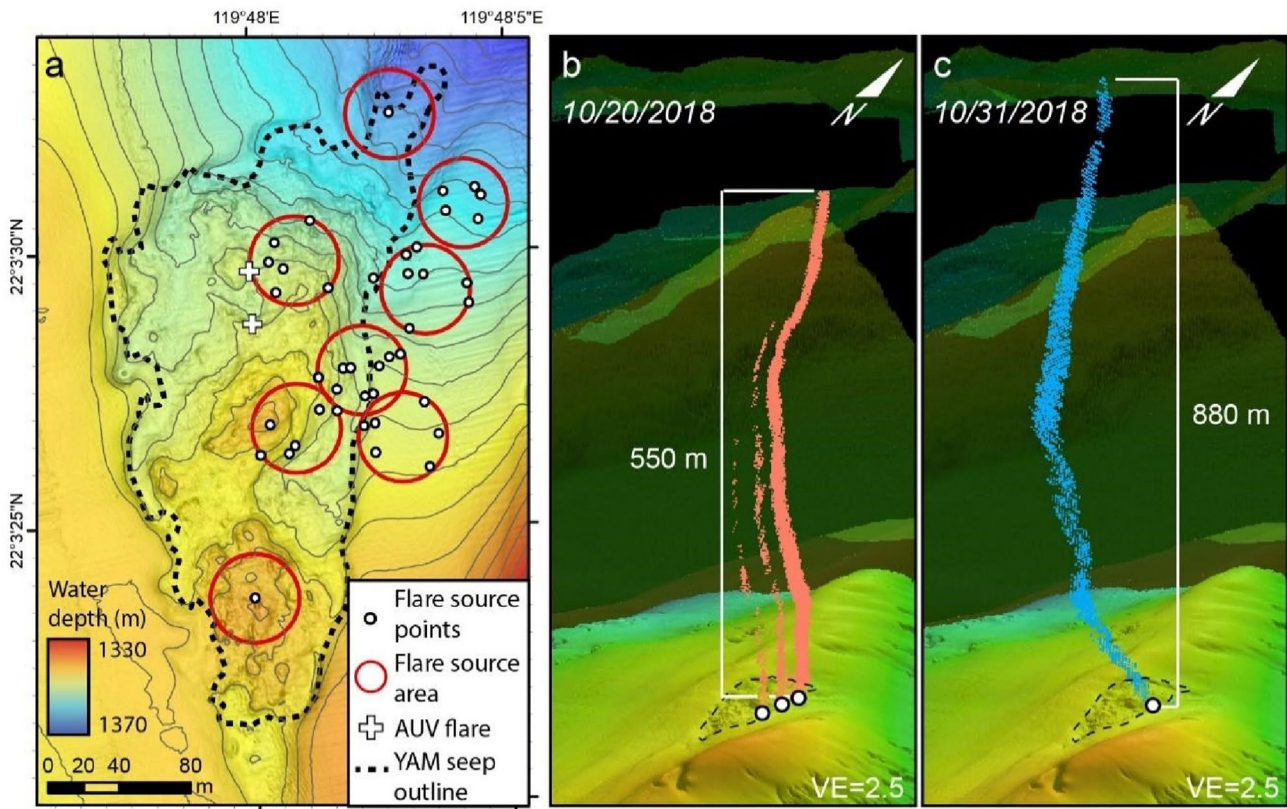**Fig. 4** Positions of gas seepage sites and shape of hydroacoustic anomalies in the water column that are diagnostic of rising gas bubbles ('flares') at the Yam Seep. **a** Positions overlying the Yam Seep.

b Perspective view from SE showing three separate flares above the northeastern rim on October 20, 2018. **c** Perspective view from SE showing one flare above the northeastern rim on October 31, 2018

Fig. 5 Ex-situ concentrations of methane dissolved in water samples taken during station GeoB23208 (4 separate casts) across the center of the Yam Seep in W–E direction on October 20, 2018 (Mau et al. 2020). Numbers at circles indicate concentrations of dissolved methane (in nmol/L) VE = 5

concentrations close to the seafloor. Water samples from about 50 m east of the seep area (CTD-2-4) showed similar concentrations ranging from ~6.0 to ~6.6 nmol/L, again with a slight decrease with decreasing water depth.

Although bottom water currents have not been investigated in this study, the relatively low CH_4 concentrations measured in water samples collected at casts CTD-2-2 and CTD-2-4 support the observation that most of seafloor gas emissions at the Yam Seep in 2018 occurred from its rim. However, seepage of methane in the dissolved phase from the northern central sector of the seep area cannot be excluded. According to seawater temperature and salinity, methane concentration in-situ atmospheric equilibrium would be 3.6 nM, but all measured concentrations were much higher. Therefore, seepage of methane in the dissolved phase is probably focused at spatially limited areas like fractures, might be temporally more variable and, thus, less significant. The cause(s) for the methane enrichments in water samples collected from the western rim of the Yam Seep (cast CTD-2-1), where no flares were observed, may be explained by (i) the presence of diffusive gas seepage sites, (ii) temporal variability of gas seepage, and (iii) lateral transport of water masses enriched in methane. It should be

noted, however, that data from a single station conducted are not representative for the entire seep area, as visual observations revealed the heterogeneity of recently active areas and carbonate precipitates partly preventing and focusing fluid flow.

Visual seafloor observations of seep indicators

Visual seafloor observation during surveys with the OFOS enabled analyzing the characteristics of seafloor deposits and distributions of hydrocarbon seep-related benthic fauna along the tracks. Constrained by the life cycle, living chemosynthetic fauna indicate recent fluid availability,

while authigenic carbonates document long-lasting (paleo)-seepage.

Properties and distributions of exposed carbonates as indicators of paleo-seepage

The general rough topography of the Yam Seep is associated with exposed carbonates, which occur widespread as crusts, and/or irregular outcrops. Carbonate crusts are relatively massive and thick carbonate formations and occasionally seem to comprise several layers (e.g., Figs. 6a and 7b) or to form comparably thin layers with smooth surfaces (e.g., Fig. 9c). Irregular shaped masses of free-standing carbonates are also seen (e.g., Fig. 6b).
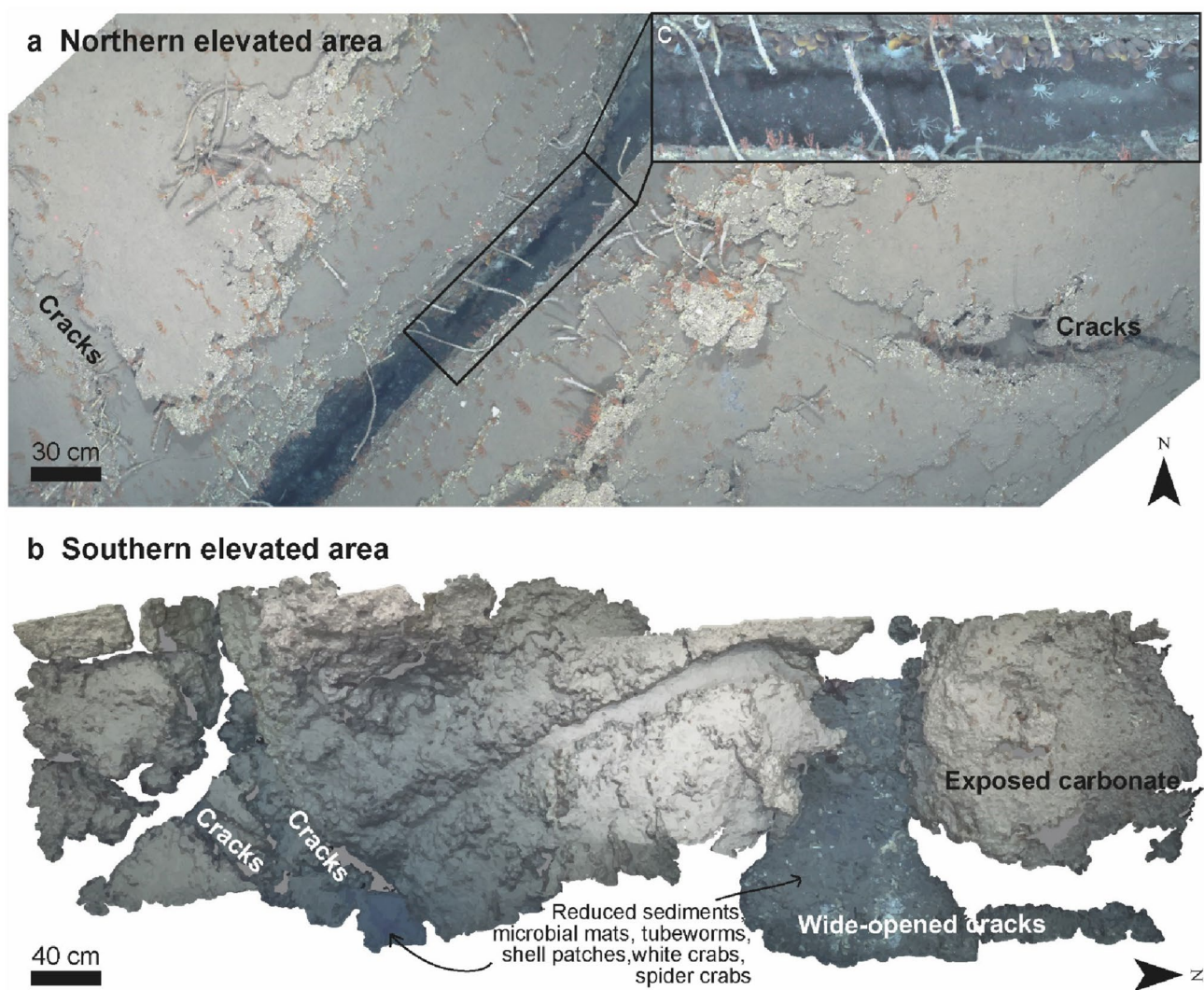

Fig. 6 Seafloor pictures taken during OFOS deployments at the Yam Seep. **a** Photomosaic of fractured carbonate crust at the northern elevated area. Individual tubeworms rooting below the carbonates. Enlarged section shows mussels, crabs, and anoxic sediments at the bottom of the fracture. Photographs taken during OFOS-2. (for exact position see Fig. 2a) **b** Orthomosaic of fractured authigenic carbonates at the southern elevated area. Anoxic sediment and fauna, including tubeworms, vesicomyid clams, galatheoid crabs and spider crabs colonized the fractures. Photographs taken during OFOS-1 (for exact position see Fig. 2a)
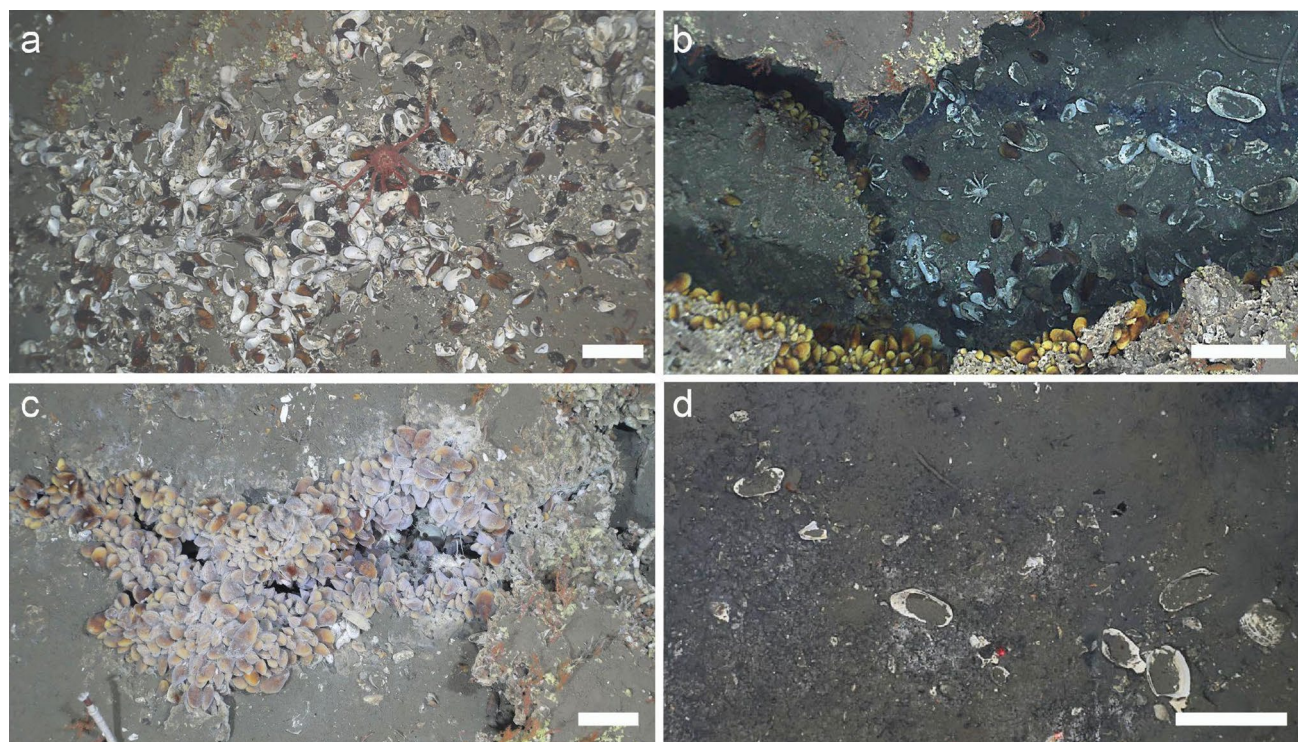
Fig. 7 Images of the seafloor taken with the OFOS at the Yam Seep (for locations see Fig. 8d). All scale bars are 20 cm. **a** Bivalve shells on a carbonate paved seafloor within a wide-opened crack in carbonate crusts. **b** Chemosynthesis-based communities clinging on the vertical wall of cracks in carbonate crusts, and dark stained (presumably anoxic) sediment on the floor of the fracture. **c** Mussels covered by microorganisms (white) within cracks of carbonate slabs. **d** Anoxic sediments and shells in an apparently poorly cemented stage

Evaluation of seafloor pictures revealed that almost all areas along the tracks hosted dense carbonate formations. Elevated areas revealed mainly flat carbonate surfaces or irregularly-formed carbonate outcrops. The southern elevated area was found to be characterized by sediment draped carbonate (Fig. 6b). Carbonate crusts were observed over a distance of several decimeters in areas of plain seafloor. Such crusts were partially draped by sediment and colonized by clams (Fig. 9c). Exposed flat carbonate crusts were dominant in elevated areas showing thick formation, including several fields of oblique thick carbonate crusts. We did not observe a clear trend in the distribution of the different types of carbonate formation as the carbonate crusts at relatively plain seafloor are less exposed. Plain areas may also be paved by flat carbonate crusts. For example, failure of sediment recovery during station GC-2 (Fig. 2) at plain seafloor (Fig. 9b) suggests the presence of hard carbonaceous substrate beneath.

Appearance and distributions of fractures in carbonates

Intense fracturing of the carbonate structures adds to the rough topography of the area. The fractures generally have an N–S orientation (Figs. 2b and c). In the AUV-derived high-resolution backscatter map, fractures can be observed at the northern and southern elevated areas as linear zones of low backscatter (Figs. 2b and c). The southern elevated area was also visually found to be characterized by fracturing (e.g., Fig. 6b). Fractures and cracks of the carbonate paved seafloor occur with different sizes and dimensions. They appear as linear troughs with steep, even vertical walls (Fig. 6a), which are likely caused by tectonic movements within the accretionary ridge, since the N-S orientation corresponds to normal faults of the structure (Kunath et al. 2020). Fractures range from ~15 to ~100 cm in width. They are more common in the center of the seep area. At the northern elevated area, a several m-long and dm-wide, SW-NE oriented fracture was discovered (Fig. 6a). Other cracks are more irregular structures with uneven walls (Fig. 6b). Therefore, the observed cracks and build-ups are interpreted as erosive structures. Cracks with variable orientations separated carbonate slabs at the northern elevated and the southern elevated area (Fig. 6b).

Along the OFOS tracks, fractures were often found to be partly filled with sediments. These are characterized by dark stained patches suggesting near-surface anoxic conditions and are presumably caused by the presence of

H$_2$S near the seafloor (Figs. 6a, b, and 7b). Such staining was not observed for sediments covering carbonate slabs (Figs. 6a and 7c). The majority of anoxic sediments were also found to host microbial mats (Fig. 8a). Microbial mats and patches of anoxic sediment occur in the entire seep area including its rim and close surroundings suggesting that fluid migration is happening in shallow sediments even outside the morphologically identified seep area. The most extensive area (> 40 m in length) characterized by the presence of dark stained sediments and microbial mats was located at the NE rim of the Yam Seep (Fig. 8a).

Chemosynthetic animals as indicators of recent seepage

Hydrocarbon seep-related animals documented at the Yam Seep include bathymodiolinae mussels (Fig. 7a–c), which harbor symbiotic chemoautotrophic bacteria (Duperron
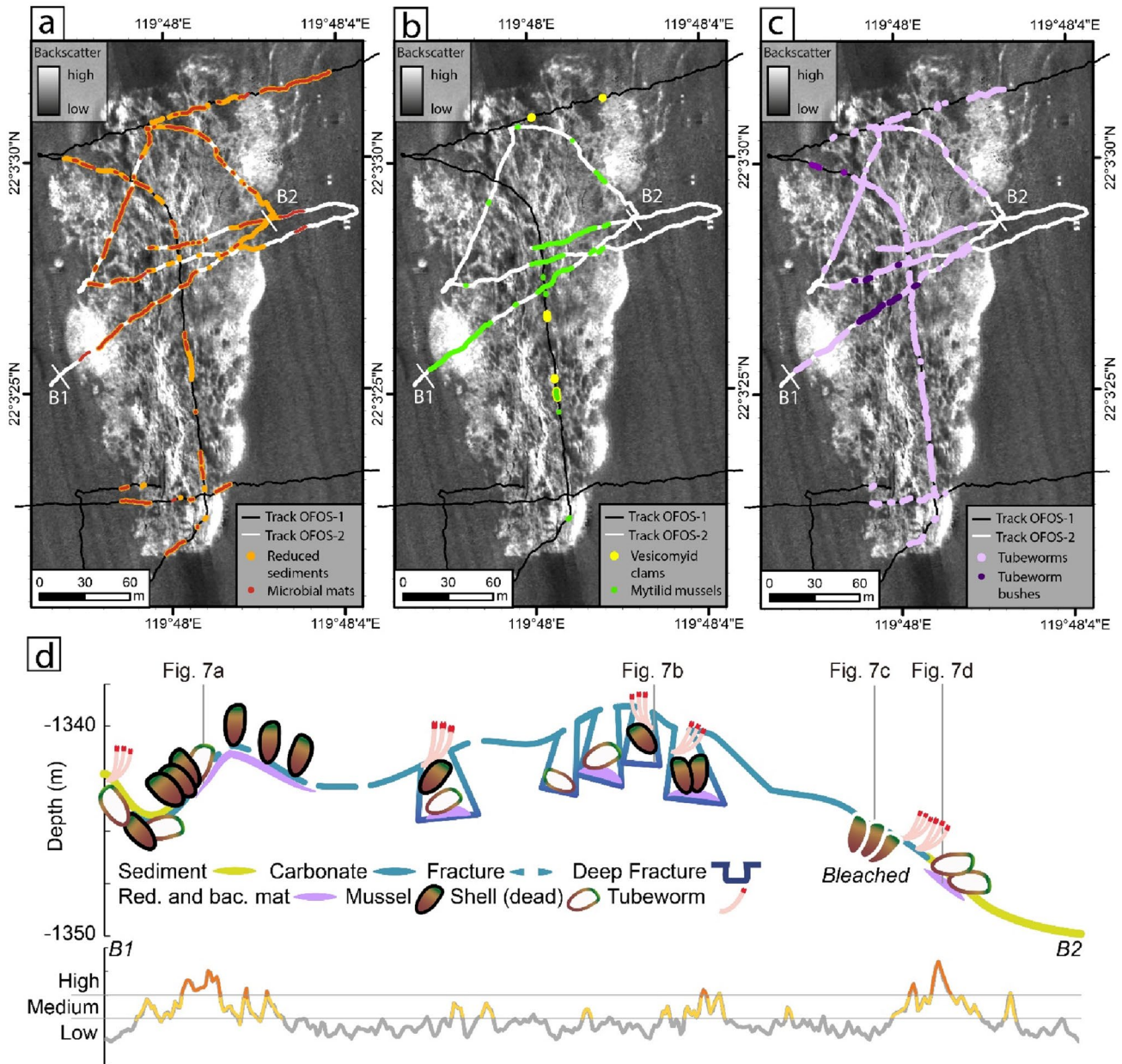
Fig. 8 Distribution of **a** anoxic sediments and microbial mats, **b** vesicomyid mussels and mytilid clams, and **c** tubeworms at the Yam Seep as observed by video footage recorded during OFOS surveys (tracks marked in white) during cruise SO266/1. **d** SW–NE section of OFOS-2 (B1–B2) crossing the central Yam Seep was studied for seep indications and backscatter intensity. Seafloor photos of specific locations along the topographic profile can be found at Fig. 7a–d
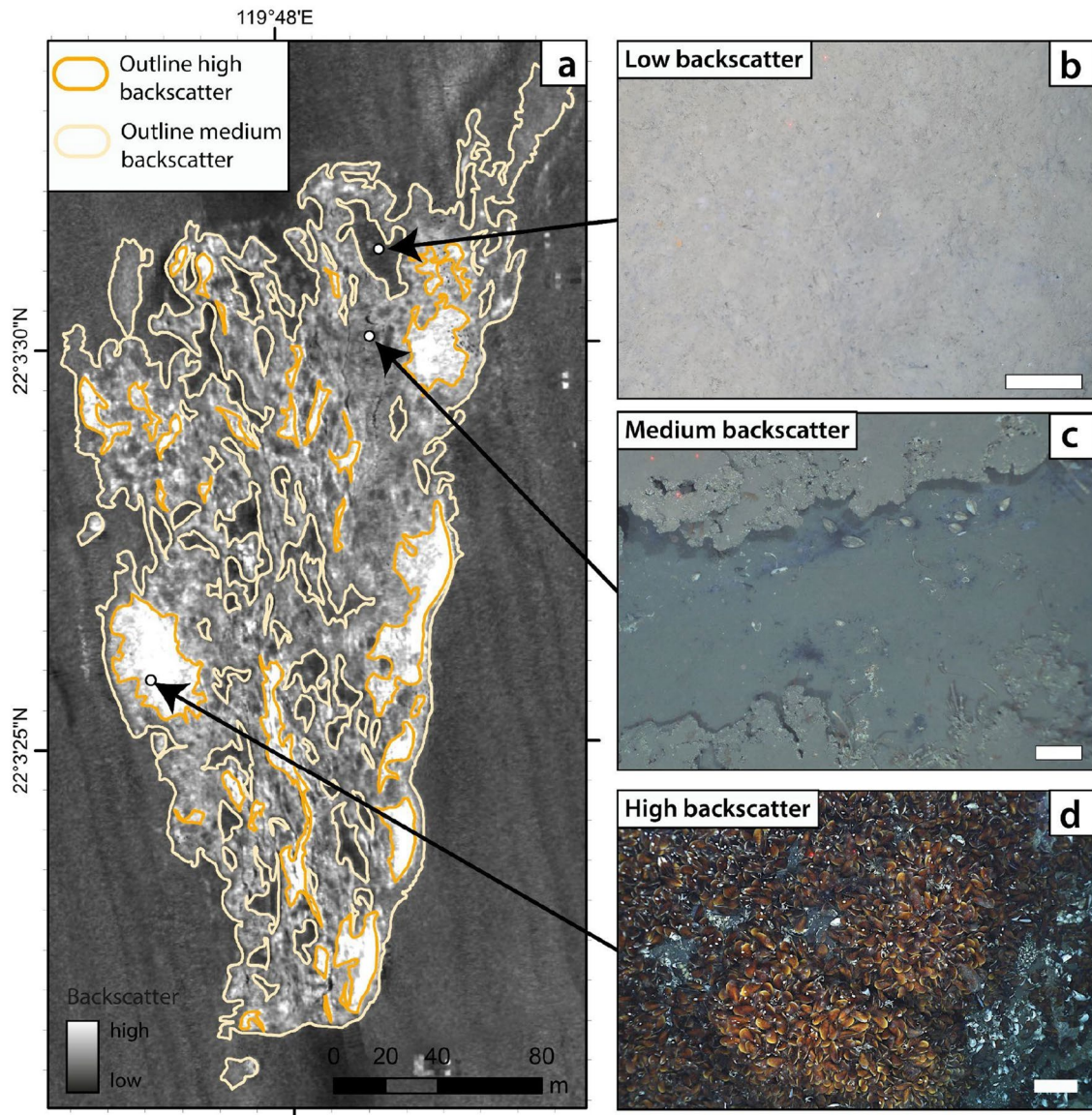
Fig. 9 **a** Seafloor backscatter map of the Yam Seep with outlines of medium and high seafloor backscatter areas. **b** Soft sediments characterize low backscatter intensities. **c** Carbonate crusts partly covered by a thin layer of sediments produce medium backscatter intensities. Clams were found to live in the sediments. **d** Dense faunal assemblages dominated by mytilid mussels and crabs covering the seafloor were seen in areas of high seafloor backscatter. White scale bar in **b**–**d** is 20 cm

et al 2005). *Gigantidas platifrons* (previously known as *Bathymodiolus platifrons*) and *Gigantidas securiformis* (formerly *Bathymodiolus securiformis)* have been reported to occur at Yam Seep (Kuo et al. 2019) and are abundant in other hydrocarbon seeps in the South China Sea as well (Wang et al. 2022). For Yam Seep, dense accumulations of mytilid mussels were discovered in the northern elevated area (Fig. 8b) at the bottom of fractures of carbonate precipitates. In the center of the seep area, mussel accumulations were also found attached to subvertical walls of fractures (Figs. 6a, 7b). Mytilid mussels were also found at the northern elevated area settling mostly within the

fractures, cracks, or clinging at the steep fracture flanks. Additional dense mussel accumulations were observed at the eastern rim of the seep area (Fig. 9d).

Apart from living mussels, the massive extent of accumulations of shells from dead mussels provides evidence of past occurrences of living mussels in a certain density, which hence indicate active seepage at the Yam Seep in the past. Shell accumulations were found in fractures of carbonates at the central and western parts of the seep area. Shell accumulations were present at the rim of the seep area and frequently found peripheral to living mussel accumulations. In some areas, a transition of dense mussel communities to

dense shell accumulations was observed and some regions were characterized by a mixture of living mussels and shells of mussels and clams (Fig. 7a). At the western rim of the Yam Seep a field containing shells was found to extend 10 m along the track of OFOS-2 (Fig. 8d). At the eastern rim, shell debris was found partly covered and buried by sediment with dark patches and potentially slightly cemented (Figs. 7d and 8d). This observation suggests the past fluid flow with dissolved methane at specific locations that sustained chemoautotroph communities, and may indicate a regional variation of the fluid transporting dissolved methane to the seafloor.

Living vesicomyid clams were barely spotted as they live buried in soft sediments. In some areas clams were seen embedded in soft sediments within fractures (Fig. 9c), e.g., at the northern and southern parts of the seep area (Fig. 8b). The presence of vesicomyid clams implies that soft sediments fill the fractures between the authigenic carbonates. The colonization at the fractures additionally suggests supply of sulfide to support the vesicomyid clam communities. Such environments have been suggested to be the precursor stage towards the capping of sediments by carbonate precipitation (Sahling et al. 2008a, b).

The occurrence of live chemoautotroph mussels and clams is key indicator for present hydrocarbon seepage. They suggest different scenarios due to the habitat requirement and chemical fuels. Whereas mussels cling to a hard substrate and use dissolved methane to fuel their symbionts, clams burrow into soft sediments percolated by hydrogen sulfide (Dubilier et al. 2008). The different settlements of mussel accumulations at the Yam Seep (surface covering in the western part and attached on vertical outcropping carbonate walls in the central area) suggest varying dissolved methane emissions depending on the carbonate structures at these different locations. Such differences can be argued to be related to the structures of the whole carbonate paved area, in which fluids with dissolved methane only occurred at a certain level. The spatial differences might be attributed to the occurrence of gas hydrate accumulations underneath the fractured carbonate slabs.

Tubeworms (polychaetes) were widely observed on carbonates (Fig. 6a). Siboglinid tubeworms live in symbiosis with chemoautotrophic, sulfur-oxidizing bacteria, are considered as one of the primary producers in seep communities (Sahling et al. 2008a, b), and have also been reported from the South China Sea at the Haima cold seep (Wang et al. 2022). Since tubeworms are sessile and can live for more than a century, their presence indicates that seepage activity has persisted for decades (Bergquist et al. 2000; Fisher et al. 1997).

At the Yam Seep, tubeworms occurred in bushes composed of up to several tens of individuals, but also of 2–3 single tubeworms only in some places (Fig. 8c). Tubeworms generally rooted below the carbonate slabs and extended out from fractures. Tubeworm bushes were mainly found associated to shallow fractures, while single tubeworms occured on isolated carbonate masses or at the edges of carbonate slabs. At a deeply incised fracture in the central part of the seep area, tubeworm bushes were attached to vertical flanks of exposed carbonate layers (Fig. 6a). Individual tubeworms were observed to reach lengths of up to ~ 1 m. The widespread occurrence of authigenic carbonates and tubeworms again substantiates the long-lasting history of gas seepage in the study area.

Other non-chemosynthetic faunal elements, such as corals and anemones, were frequently observed attached to carbonates and along fractures. Such animals might not indicate seepage, but indicate the long-term exposition of the carbonate precipitate as hard ground for settlement and nutrients supply through water currents (Deng et al. 2019; Hovland and Risk 2003; Wang et al. 2022). Other mobile animals such as galatheoid crabs or spider crabs were widely found close to or within the fauna communities of the seep area. Such an abundance of organisms suggests a sufficient food source.

Seafloor backscatter characteristics related to the seep system

Joint evaluation of the bathymetric and seafloor backscatter data together with visual seafloor observation enabled a spatial correlation of seafloor deposit characteristics and faunal distribution (Fig. 9a–d). Sediment draped areas correlate with relatively smooth seafloor as indicated by the smooth topography and low backscatter intensities (Fig. 9b). The different backscatter intensities of carbonate covered and fractured areas seem to be caused by the density of colonization by clams as observed at a site characterized by medium intensity (Fig. 9c). High backscatter intensities were also detected in areas colonized by living mytilid mussels (Fig. 9d).

Not all mytilid mussel accumulations observed along the OFOS tracks are associated with high backscatter intensity, for instance when located within deeply incised fractures or partly covered by sediments. Numerous sites with chemosynthesis-based communities, including extensive accumulations of shells from vesicomyid clams (Fig. 7a), mytilid mussels (Fig. 7c), and mytilid mussels attached to vertical fracture walls (Fig. 7b) were observed during the seafloor visual survey (OFOS-2) in the central elevated area (Fig. 8d). At the eastern rim, an extensive area with dark stained sediments adjacent to a field of shell accumulations, which mostly correlate to high backscatter characteristics, has been observed. At the western periphery, shells were seen to be covered by sediments (Fig. 7d).

According to our observations we conclude that (i) high backscatter intensities areas are mostly related to shells and

living mytilid mussels; (ii) medium backscatter intensity correspond to authigenic carbonates partly hosting chemosynthesis-based communities; (iii) low backscatter relates to soft sediments (even when covering authigenic carbonates in greater depth). Backscatter intensity of shells or fractures is strongly affected (reduced) by sediment draping.

The backscatter intensities recorded within the seep area are not homogeneous, but widely scatter and range from low to high (Fig. 9a). Most of the seep area is characterized by medium backscatter intensities ($> 70\%$), which separates the seep area to the surrounding seafloor of homogeneously low backscatter. Low backscatter areas also occur within the seep area, but account for $< 15\%$ of the total seep area and occur as relatively small areas throughout the entire area (maximum < 500 m^2). About 15% of the seep area is characterized by high backscatter, with the largest coherent areas covering ~ 1000 m^2.

Evolution of the Yam Seep

Swath-bathymetry, side-scan sonar imaging, and OFOS seafloor imagery showed that the seafloor topography of the active YAM seep system is dominated by authigenic carbonate. The carbonate precipitates, which are the result of AOM, are either exposed or covered by thin layers of sediments. The presence of intensely fractured authigenic carbonates suggest that formation and exposure of the Yam Seep on top of the FWCR anticline is strongly controlled by tectonic compression, uplifting of the accretionary ridge, gas migration and seafloor seepage, and focused seafloor erosion. Ongoing AOM results in the formation of authigenic carbonates and sediment cementation (Bayon et al. 2009; Hovland 2002). Further carbonate precipitation at newly developed gas emission pathways expands the carbonate paved area (Liebetrau et al. 2014; Loher et al. 2018). Gas bubble discharge recorded in 2013, 2017, and 2018 along with seawater methane enrichments measured in 2018 indicate that (i) the Yam Seep is an actively methane seeping area and (ii) up to meter-thick carbonate pavements result from long-term seepage. Seepage areas characterized by similar features have been documented in other active margins at accretionary ridges, i.e. Hydrate Ridge (Teichert et al. 2005; Paull et al. 2015) and offshore southern Nicaragua, both linked to underlying fault systems (Moerz et al. 2005; Sahling et al. 2008a, b).

Tectonic movements like thrusting and uplifting of the submarine ridge potentially cause the fracturing and exposure of the seep region. Erosion at slump scars was observed at FWCR, which were reported as the results of over-tilting of the uplifting ridge (Chen et al. 2020a, b; Klaucke et al. 2016). In addition to tectonic influence, we argue that seafloor erosion due to currents and biology might have been involved in shaping the Yam Seep. Stronger currents result

in unconsolidated sediment being carried away, exposing the consolidated authigenic carbonates on the seafloor which in general formed hardgrounds for filter-feeder fauna. Internal waves (Alford et al. 2015) were reported to occur peripheral to FWCR at canyons adjacent to the upper slope and shelf, and especially related to records of Penghu canyon (Klaucke et al. 2016; Kunath et al. 2020; Yu and Chang 2002), which effect the region including our study area by scavenging on the surface sediments. Bioerosion is also a potential erosion force in our study area as we observed abundant chemosynthetic animals along or within the edge of cracks (Paull et al. 2005).

Beside tectonic processes affecting seepage sites, the formation of gas hydrates in shallow sediments can have an important influence on the seep evolution, especially when gas bubbles are emanating at the seafloor (Marcon et al. 2014). Since the Yam Seep is located well within the gas hydrate stability zone, gas upward migration would lead to the deposition of gas hydrate (Sloan and Koh 2007) underneath the exposed carbonates. Examples from several studies reported wide areas of updoming or collapsing of carbonate paved seafloor related to gas hydrate accumulation or dissociation (Matsumoto et al. 2009; Sahling et al. 2008a, b). A good example was described from the Calabrian arc in the Mediterranean Sea where massive gas hydrate below a thin carbonate crust was dissolved and the carbonate crust collapsed (Loher et al. 2018). Methane migrated below the cemented and sealed layer of precipitated authigenic carbonates, where it formed massive gas hydrates in contact with water. An accumulation of gas hydrate at such shallow sediment depth inhibits an increased buoyancy but also could push the overlying sediments up (Barry et al. 2012). Because the Yam Seep is situated ~ 700 m below the upper boundary of the gas hydrate stability zone (GHSZ) and above the lower boundary of GHSZ at ~ 650 mbsl marked by a bottom simulation seismic reflector (Kunath et al. 2020). Thermal and pressure effects by glacial/interglacial changes which move the seafloor and shallow sediments out of the stability zone can be neglected.

The local presence of gas hydrates is causing a heterogeneous supply of methane available for chemosynthesis-based habitats. Clams and microbes found within shallow fractures at relatively smooth areas and covered by sediment suggest that the area and close surroundings are characterized by methane supply. Tubeworms are commonly found adhering to carbonate crusts of different sizes and shapes, and prove that seepage has been around for a longer time. Mytilid mussels suggest a later stage of seepage when carbonate hard ground are available where mytilid larvae initially can settled down and benefit from the dissolved methane-rich bottom which they use for their metabolism and thrive via their microbes in the gills (Sibuet and Olu 1998). Corals colonizing carbonate build-ups were found frequently over

the paved area, indicating that nutrients were sufficiently available for filter-feeders and that bottom water currents most likely exposed the hard carbonate substrates (Hovland and Risk 2003; Roberts et al. 2009).

Summarizing our results presented in this study, we established a simplified conceptual model with four evolutionary stages (Fig. 10) in order to discuss the dominant processes at the Yam Seep:

Stages I and II—initial seepage and carbonate precipitation

Initially light hydrocarbons begin to migrate along permeable fault networks to the shallow subsurface. When methane comes in contact with seawater-derived sulfate, AOM produces sulfide and initiates formation of authigenic

Fig. 10 Schematic model of the evolution of the Yam Seep compiling the results of this study

carbonates. The sulfide-rich environment enables colonization by vesicomyid clams. Tubeworms can settle on authigenic carbonates that serve as hard substrates (Cordes et al. 2003, 2005; Freytag et al. 2001; Sahling et al. 2008a, b).

Stage III—increasing precipitation and seafloor sealing

The continued supply of methane enhances the density of authigenic carbonates and the formation of carbonate slabs that increasingly seal the seafloor and deflect upward migration fluids. Gas hydrate (blue gradient shaded hexagons in Fig. 10) formation underneath the carbonate slabs may also be induced. Near-seafloor carbonates and gas hydrates hamper fluid upward migration and direct gas escape from the seafloor at Yam Seep. Instead, deflection of fluids towards the edges of the carbonate crust causes lateral growth of the seep-influenced area as suggested by the sporadic occurrence of carbonate chunks in hemipelagic sediments at the peripheral sites GC-4 and GC-8. Chemosynthetic organisms settle at the rim of the seep area, where gas migrates through higher permeability sediments.

Stage IV—erosion and re-shaping of seafloor morphology

Partial exposure of the paved carbonate area, fracturing of carbonate slabs, and fauna colonization occur. We postulate that tectonic movement causes ridge uplifting, sediment removal through marine erosional processes along tilted flanks and exposure of carbonate crusts. Thrusting and faulting affect the cemented carbonate slab and cause fracturing and opening of pathways for gas ebullition. Repeated sealing within cracks and fracturing of the lower cemented crusts shaped the (a) deeply fractured crusts. Meanwhile, (b) carbonate precipitation occurs in the exposed sediments at the more profound depth within deep fracture. (c) Free gas migrates along the extensional fault and is partly released from the sediment to the water column. However, part of the free gas gets trapped underneath the carbonate crusts and potentially forms gas hydrate, which fuels chemosynthesis-based communities. Peripheral to the carbonate area, fractured crusts buried in shallow sediment (d) and anoxic sediment (e) experience the processes of stage I to III. Because of blocking, new migration and seepage pathways evolve, which consequently extend the carbonate paved area. Anoxic sediments and the presence of vesicomyid clams living in sediments within fractures are the key features occurring at the rim and the relatively plain regions.
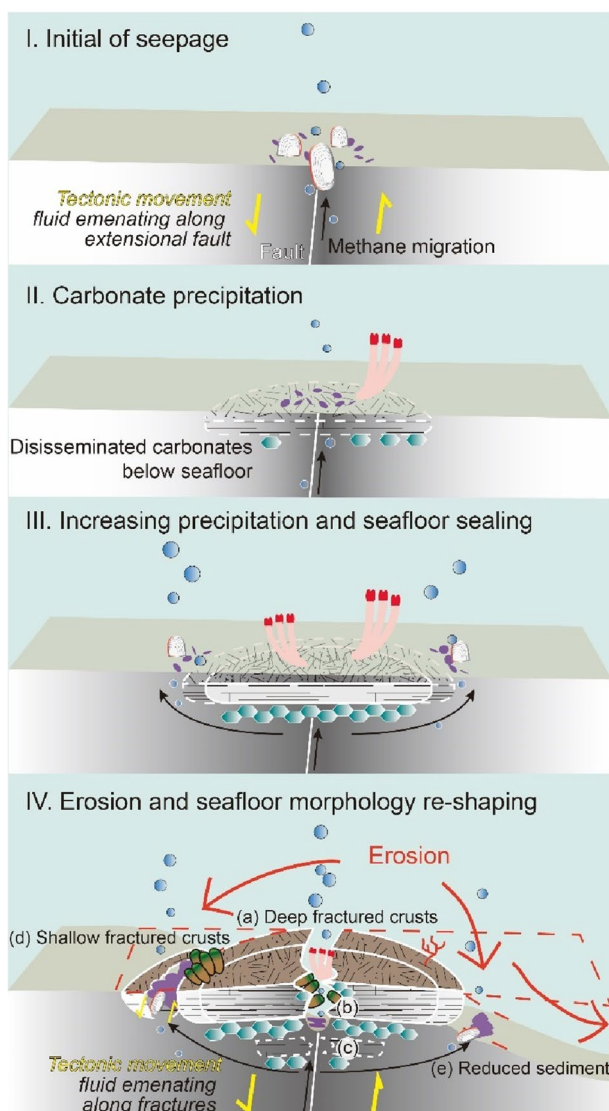
Conclusions

In addition to previous seismic and side-scan sonar studies since 2013, our study constrains the geological processes that control the formation of the Yam Seep and characterizes the carbonate-cemented, fractured, and exposed region. Hydro-acoustic data documented several flare sightings, defined eight source areas for recent gas bubble ebullition at the center and the eastern flank of the Yam Seep, and illustrated its spatial and temporal variability. The seafloor backscatter results reveal the seafloor characteristics with the highest backscatter intensity related to shell distribution and middle-intensity-patterns to fractures and cracks. Enrichments of dissolved methane were found at the rim of the seep area. Ample seep-related and widespread fauna was observed visually. The widespread occurrence of authigenic carbonates illustrates the long-term seep evolution while the presence of living chemosynthesis-based community suggests recent hydrocarbon seep activity.

The diverse evidence observed at the Yam Seep was used to propose an active margin seep area evolution under dynamic tectonic conditions, geochemical, and biological interaction, involving four stages: (I) Initial seafloor seepage of methane, (II) Carbonate precipitation, (III) Increasing precipitation and seafloor sealing, (IV) Erosion and seafloor morphology re-shaping. Stages I–III relate to the geochemical process of methane seepage and carbonate precipitation and its indicator fauna. Stage IV includes the exposure of the seep carbonates under tectonic faulting, uplifting, over-tilting and the expansion of the seep area with repeating stages I–III at its periphery.

Data availability statement Relevant data are made available through the World Data Center PANGAEA® (http://www.pangaea.de). Additional information is available to interested readers on request.

Declarations

Conflict of interest The authors declare that they have no known competing financial interests or personal relationships that could have appeared to affect the work reported in this paper.

References

Alford MH, Peacock T, MacKinnon JA, Nash JD, Buijsman MC, Centurioni LR, Chao S-Y, Chang M-H, Farmer DM, Fringer OB, Fu K-H, Gallacher PC, Graber HC, Helfrich KR, Jachec SM, Jackson CR, Klymak JM, Ko DS, Jan S, Shaun Johnston TM, Legg S, Lee IH, Lien R-C, Mercier MJ, Moum JN, Musgrave R, Park J-H, Pickering AI, Pinkel R, Rainville L, Ramp SR, Rudnick DL, Sarkar S, Scotti A, Simmons HL, St Laurent LC, Venayagamoorthy SK, Wang Y-H, Wang J, Yang YJ, Paluszkiewicz T, Tang T-Y (2015) The formation and fate of internal waves in the South China Sea. Nature 521:65–69. https://doi.org/10.1038/nature14399

Barry MA, Boudreau BP, Johnson BD (2012) Gas domes in soft cohesive sediments. Geology 40:379–382. https://doi.org/10.1130/G32686.1

Bayon G, Henderson GM, Bohn M (2009) U-Th stratigraphy of a cold seep carbonate crust. Chem Geol 260:47–56. https://doi.org/10.1016/j.chemgeo.2008.11.020

Bergquist DC, Williams FM, Fisher CR (2000) Longevity record for deep-sea invertebrate. Nature 403:499–500. https://doi.org/10.1038/35000647

Berner RA (1990) Atmospheric carbon dioxide levels over phanerozoic time. Science 249:1382–1386. https://doi.org/10.1126/science.249.4975.1382

Berner RA, Raiswell R (1983) Burial of organic carbon and pyrite sulfur in sediments over phanerozoic time: a new theory. Geochim Cosmochim Acta 47:855–862. https://doi.org/10.1016/0016-7037(83)90151-5

Boetius A, Ravenschlag K, Schubert CJ, Rickert D, Widdel F, Gieseke A, Amann R, Jørgensen BB, Witte U, Pfannkuche O (2000) A marine microbial consortium apparently mediating anaerobic oxidation of methane. Nature 407:623–626. https://doi.org/10.1038/35036572

Bohrmann G, Greinert J, Suess E, Torres M (1998) Authigenic carbonates from the Cascadia subduction zone and their relation to gas hydrate stability. Geology 26:647–650. https://doi.org/10.1130/0091-7613(1998)026%3c0647:ACFTCS%3e2.3.CO;2

Bohrmann G, Ahrlich F, Bergenthal M, Berndt C, Chen J, Chen S, Chen T, Chen W, Chi W, Deusner C, Elger J, Freudenthal T, Fröhlich S, Klein T, Kramer L, Kuhnert M, Fan L, Hsu H, Lai M, Lin S, Lin T, Mai H, Mau S, Malnati J, Meyer-Schack B, Niederbockstrut B, Pape T, Rosiak U, Stachowski A, Stamp A, Tseng Y, Tu T, Wallmann K, Wang Y, Wetzel G, Wei K, Wintersteller P, Wu Y, Wunsch D, Yu P (2019) R/V SONNE cruise report SO266/1, MeBo200 Methane Hydrate Drillings Southwest of Taiwan, TaiDrill, Cruise No. 266/1, 15 October—18 November 2018, Kaohsiung (Taiwan)—Kaohsiung (Taiwan). SONNE-Berichte; SO266/1; 1–201. https://doi.org/10.48433/cr_so266_1

Bohrmann G, Heeschen K, Jung C, Weinrebe W, Baranov B, Cailleau B, Heath R, Hühnerbach V, Hort M, Masson D (2002) Widespread fluid expulsion along the seafloor of the Costa Rica convergent margin. Terra Nova 14:69–79. https://doi.org/10.1046/j.1365-3121.2002.00400.x

Borowski WS, Paull CK, Ussler W III (1996) Marine pore-water sulfate profiles indicate in situ methane flux from underlying gas hydrate. Geology 24:655–658. https://doi.org/10.1130/0091-7613(1996)024%3c0655:MPWSPI%3e2.3.CO;2

Bowin C, Lu RS, Lee C-S, Schouten H (1978) Plate convergence and accretion in Taiwan-Luzon region. AAPG Bull 62:1645–1672. https://doi.org/10.1306/C1EA5260-16C9-11D7-8645000102C1865D

Caress DW, Chayes DN (1996) Improved processing of Hydrosweep DS Multibeam Data on the *R/V Maurice Ewing*. Mar Geophys Res 18:631–650. https://doi.org/10.1007/BF00313878

Caress DW, Thomas H, Kirkwood WJ, McEwen R, Henthorn R, Clague DA, Paull CK, Paduan J, Maier KL (2008) High-resolution multibeam, sidescan, and subbottom surveys using the MBARI AUV D. Allan B. In: Reynolds JR, Greene HG (eds) Marine habitat mapping technology for Alaska. Alaska Sea Grant College Program, University of Alaska Fairbanks, Fairbanks. https://doi.org/10.4027/mhmta.2008.04

Chen S-C, Hsu S-K, Wang Y, Chung S-H, Chen P-C, Tsai C-H, Liu C-S, Lin H-S, Lee Y-W (2014) Distribution and characters of the mud diapirs and mud volcanoes off southwest Taiwan. J Asian Earth Sci 92:201–214. https://doi.org/10.1016/j.jseaes.2013.10.009

Chen NC, Yang TF, Hong WL, Chen HW, Chen HC, Hu CY, Huang YC, Lin S, Lin LH, Su CC (2017) Production, consumption, and migration of methane in accretionary prism of southwestern Taiwan. Geochem Geophys Geosyst 18:2970–2989. https://doi.org/10.1002/2017GC006798

Chen N-C, Yang TF, Hong W-L, Yu T-L, Lin I-T, Wang P-L, Lin S, Su C-C, Shen C-C, Wang Y, Lin L-H (2020a) Discharge of deeply rooted fluids from submarine mud volcanism in the Taiwan accretionary prism. Sci Rep 10:381. https://doi.org/10.1038/s41598-019-57250-9

Chen T-T, Paull CK, Liu C-S, Klaucke I, Hsu H-H, Su C-C, Gwiazda R, Caress DW (2020b) Discovery of numerous pingos and comet-shaped depressions offshore southwestern Taiwan. Geo-Mar Lett 40:407–421. https://doi.org/10.1007/s00367-019-00577-z

Chuang PC, Yang T, Hong WL, Lin S, Sun CH, Lin AS, Chen JC, Wang Y, Chung SH (2010) Estimation of methane flux offshore SW Taiwan and the influence of tectonics on gas hydrate accumulation. Geofluids 10:497–510. https://doi.org/10.1111/j.1468-8123.2010.00313.x

Chuang PC, Dale AW, Wallmann K, Haeckel M, Yang TF, Chen NC, Chen HC, Chen HW, Lin S, Sun CH (2013) Relating sulfate and methane dynamics to geology: accretionary prism offshore SW Taiwan. Geochem Geophys Geosyst 14:2523–2545. https://doi.org/10.1002/ggge.20168

Chuang P-C, Yang TF, Wallmann K, Matsumoto R, Hu C-Y, Chen H-W, Lin S, Sun C-H, Li H-C, Wang Y, Dale AW (2019) Carbon isotope exchange during anaerobic oxidation of methane (AOM) in sediments of the northeastern South China Sea. Geochim Cosmochim Acta 246:138–155. https://doi.org/10.1016/j.gca.2018.11.003

Claypool GE, Kaplan I (1974) The origin and distribution of methane in marine sediments. In: Kaplan IR (ed) Natural gases in marine sediments. Marine science, vol 3. Springer, Boston, pp 99–139. https://doi.org/10.1007/978-1-4684-2757-8_8

Cordes EE, Bergquist DC, Shea K, Fisher CR (2003) Hydrogen sulfide demand of long-lived vestimentiferan tube worm aggregations modifies the chemical environment at deep-sea hydrocarbon seeps. Ecol Lett 6:212–219. https://doi.org/10.1046/j.1461-0248.2003.00415.x

Cordes EE, Arthur MA, Shea K, Arvidson RS, Fisher CR (2005) Modeling the mutualistic interactions between tubeworms and microbial consortia. PLoS Biol 3:e77. https://doi.org/10.1371/journal.pbio.0030077

Dadson SJ, Hovius N, Chen H, Dade WB, Hsieh M-L, Willett SD, Hu J-C, Horng M-J, Chen M-C, Stark CP, Lague D, Lin J-C (2003) Links between erosion, runoff variability and seismicity in the Taiwan orogen. Nature 426:648–651. https://doi.org/10.1038/nature02150

Deng Y, Chen F, Li N, Jin M, Cao J, Chen H, Zhou Y, Wu C, Zhuang C, Zhao Y, Cheng S (2019) Cold-water corals in gas hydrate drilling cores from the South China Sea: occurrences, geochemical characteristics and their relationship to methane seepages. Minerals 9:742. https://doi.org/10.3390/min9120742

Dubilier N, Bergin C, Lott C (2008) Symbiotic diversity in marine animals: the art of harnessing chemosynthesis. Nat Rev Microbiol 6:725–740. https://doi.org/10.1038/nrmicro1992

Duperron S, Nadalig T, Caprais J-C, Sibuet M, Fiala-Médioni A, Amann R, Dubilier N (2005) Dual symbiosis in a *Bathymodiolus* sp. mussel from a methane seep on the Gabon continental margin (Southeast Atlantic): 16S rRNA phylogeny and distribution of the symbionts in gills. Appl Environ Microbiol 71:1694–1700. https://doi.org/10.1128/AEM.71.4.1694-1700.2005

Fan LF, Lin S, Hsu C-W, Tseng Y-T, Yang T, Huang K-M (2018) Formation and preservation of authigenic pyrite in the methane dominated environment. Deep Sea Res Part I 138:60–71. https://doi.org/10.1016/j.dsr.2018.07.004

Feng D, Qiu JW, Hu Y, Peckmann J, Guan HX, Tong HP, Chen C, Chen JX, Gong SG, Li N, Chen DF (2018a) Cold seep systems in the South China Sea: an overview. J Asian Earth Sci 168:3–16. https://doi.org/10.1016/j.jseaes.2018.09.021

Feng JX, Yang SX, Liang JQ, Fang YX, He YL, Luo M, Chen DF (2018b) Methane seepage inferred from the porewater geochemistry of shallow sediments in the Beikang Basin of the southern South China Sea. J Asian Earth Sci 168:77–86. https://doi.org/10.1016/j.jseaes.2018.02.005

Fisher CR, Urcuyo IA, Simpkins MA, Nix E (1997) Life in the slow lane: growth and longevity of cold-seep vestimentiferans. Mar Ecol 18:83–94. https://doi.org/10.1111/j.1439-0485.1997.tb00428.x

Freytag JK, Girguis PR, Bergquist DC, Andras JP, Childress JJ, Fisher CR (2001) A paradox resolved: sulfide acquisition by roots of seep tubeworms sustains net chemoautotrophy. Proc Natl Acad Sci USA 98:13408. https://doi.org/10.1073/pnas.23158949

Fujikura K, Tsuchida S, Huang C-Y, Nunoura T, Lin L-H, Soh W, Lin S, Machiyama H (2007) Vent-type chemosynthetic community associated with methane seep at the Formosa Ridge, off southwest Taiwan. ICGH, Taipei. In: Proceedings of the international conference on gas hydrate energy, climate and environment, p 30–31

Greinert J, Lewis KB, Bialas J, Pecher IA, Rowden A, Bowden DA, De Batist M, Linke P (2010) Methane seepage along the Hikurangi Margin, New Zealand: Overview of studies in 2006 and 2007 and new evidence from visual, bathymetric and hydroacoustic investigations. Mar Geol 272:6–25. https://doi.org/10.1016/j.margeo.2010.01.017

Han X, Suess E, Huang Y, Wu N, Bohrmann G, Su X, Eisenhauer A, Rehder G, Fang Y (2008) Jiulong methane reef: Microbial mediation of seep carbonates in the South China Sea. Mar Geol 249:243–256. https://doi.org/10.1016/j.margeo.2007.11.012

Hovland M (2002) On the self-sealing nature of marine seeps. Cont Shelf Res 22:2387–2394. https://doi.org/10.1016/S0278-4343(02)00063-8

Hovland M, Risk M (2003) Do Norwegian deep-water coral reefs rely on seeping fluids? Mar Geol 198:83–96. https://doi.org/10.1016/S0025-3227(03)00096-3

Judd A, Hovland M (2009) Seabed fluid flow: the impact on geology, biology and the marine environment. Cambridge University Press, Cambridge

Kastner M, Solomon E, Harris R, Torres M (2014) Fluid origins, thermal regimes, and fluid and solute fluxes in the forearc of subduction zones. In: Stein R, Blackman DK, Inagaki F, Larsen H-C (eds) Developments in marine geology, vol 7. Elsevier, Amsterdam, pp 671–733. https://doi.org/10.1016/B978-0-444-62617-2.00022-0

Klaucke I, Sahling H, Weinrebe W, Blinova V, Bürk D, Lursmanashvili N, Bohrmann G (2006) Acoustic investigation of cold seeps offshore Georgia, eastern Black Sea. Mar Geol 231:51–67. https://doi.org/10.1016/j.margeo.2006.05.011

Klaucke I, Berndt C, Crutchley G, Chi W-C, Lin S, Muff S (2016) Fluid venting and seepage at accretionary ridges: the Four Way Closure Ridge offshore SW Taiwan. Geo-Mar Lett 36:165–174. https://doi.org/10.1007/s00367-015-0431-5

Kunath P, Chi W-C, Berndt C, Chen L, Liu C-S, Kläschen D, Muff S (2020) A shallow seabed dynamic gas hydrate system off SW Taiwan: Results from 3-D seismic, thermal, and fluid migration analyses. J Geophys Res Solid Earth 125:e2019JB019245-T. https://doi.org/10.1029/2019JB019245

Kuo M-Y, Kang D-R, Chang C-H, Chao C-H, Wang C-C, Chen H-H, Su C-C, Chen H-W, Lai M-C, Lin S, Liu L-L (2019) New records of three deep-sea *Bathymodiolus* mussels (Bivalvia: Mytilida: Mytilidae) from hydrothermal vents and cold seeps in Taiwan. J Mar Sci Technol 27:352–358. https://doi.org/10.6119/JMST.201908_27(4).0006

Liang Q, Hu Y, Feng D, Peckmann J, Chen L, Yang S, Liang J, Tao J, Chen D (2017) Authigenic carbonates from newly discovered active cold seeps on the northwestern slope of the South China Sea: Constraints on fluid sources, formation environments, and seepage dynamics. Deep Sea Res Part I 124:31–41. https://doi.org/10.1016/j.dsr.2017.04.015

Liebetrau V, Augustin N, Kutterolf S, Schmidt M, Eisenhauer A, Garbe-Schönberg D, Weinrebe W (2014) Cold-seep-driven carbonate deposits at the Central American forearc: contrasting evolution and timing in escarpment and mound settings. Int J Earth Sci 103:1845–1872. https://doi.org/10.1007/s00531-014-1045-2

Lin S, Lim YC, Liu C-S, Yang TF, Chen Y-G, Machiyama H, Soh W, Fujikura K (2007) Formosa Ridge, A cold seep with densely populated chemosynthetic community in the passive margin, southwest of Taiwan. Goldschmidt Conf Cologne, Geochim Cosmochim Acta 71(15):A582–A582

Liu C-S, Huang IL, Teng LS (1997) Structural features off southwestern Taiwan. Mar Geol 137:305–319. https://doi.org/10.1016/S0025-3227(96)00093-X

Liu C-S, Schnurle P, Wang Y, San-Hsiung C, Song-Chuen C, Hsiuan T-H (2006) Distribution and characters of gas hydrate offshore of southwestern Taiwan. TAO Terr Atmos Ocean Sci 17:615–644

Loher M, Marcon Y, Pape T, Römer M, Wintersteller P, dos Santos FC, Praeg D, Torres M, Sahling H, Bohrmann G (2018) Seafloor sealing, doming, and collapse associated with gas seeps and authigenic carbonate structures at Venere mud volcano, Central Mediterranean. Deep Sea Res Part 1 Oceanogr Res Pap 137:76–96. https://doi.org/10.1016/j.dsr.2018.04.006

MacAvoy SE, Carney RS, Fisher CR, Macko SA (2002) Use of chemosynthetic biomass by large, mobile, benthic predators in the Gulf of Mexico. Mar Ecol Prog Ser 225:65–78. https://doi.org/10.3354/meps225065

MacDonald IR, Reilly JF, Guinasso NL, Brooks JM, Carney RS, Bryant WA, Bright TJ (1990) Chemosynthetic mussels at a brine-filled pockmark in the northern Gulf of Mexico. Science 248:1096–1099. https://doi.org/10.1126/science.248.4959.1096

Machiyama H, Lin S, Fujikura K, Huang C-Y, Ku C-Y, Lin LH, Morita S, Nunoura T, Soh W, Toki T, Yang TF (2007) Discovery of "hydrothermal" chemosynthetic community in a cold seep environment, Formosa Ridge: eafloor observation results from first ROV cruise, off Southwestern Taiwan. EOS Trans. AGU, 88 (52), Fall Meet. Suppl., Abstract OS23A-1041

Marcon Y, Ondréas H, Sahling H, Bohrmann G, Olu K (2014) Fluid flow regimes and growth of a giant pockmark. Geology 42(1):63–66. https://doi.org/10.1130/G34801.1

Matsumoto R, Okuda Y, Hiruta A, Tomaru H, Takeuchi E, Sanno R, Suzuki M, Tsuchinaga K, Ishida Y, Ishizaki O, Takeuchi R, Komatsubara J (2009) Formation and collapse of gas hydrate deposits in high methane flux area of the Joetsu Basin, eastern margin of Japan Sea. Chigaku Zasshi (j geogr) 118:43–71

Mau S, Tu T-H, Becker M, dos Santos FC, Chen J-N, Lin L-H, Wang P-L, Lin S, Bohrmann G (2020) Methane seeps and independent methane plumes in the South China Sea offshore Taiwan. Front Mar Sci 7:543. https://doi.org/10.3389/fmars.2020.00543

Moerz T, Fekete N, Kopf A, Brückmann W, Kreiter S, Hühnerbach V, Masson D, Hepp D, Schmidt M, Kutterolf S, Sahling H, Abegg F, Spiess V, Suess E, Ranero CR (2005) Styles and productivity of mud diapirism along the Middle American margin. Part II: Mound Culebra and Mounds 11, and 12. In: Martinelli G, Panahi B (eds) Mud volcanoes, geodynamics and seismicity. NATO science series, vol 51. Springer, Dordrecht, pp 40–76. https://doi.org/10.1007/1-4020-3204-8_5

Naehr TH, Eichhubl P, Orphan VJ, Hovland M, Paull CK, Ussler W, Lorenson TD, Greene HG (2007) Authigenic carbonate formation at hydrocarbon seeps in continental margin sediments: a comparative study. Deep-Sea Res Part II Top Stud Oceanogr 54:1268–1291. https://doi.org/10.1016/j.dsr2.2007.04.010

Pape T, Bohrmann G (2022) Shallow gas hydrates associated to pockmarks in the Northern Congo Deep-Sea Fan, SW Africa. In: Mienert J, Berndt C, Tréhu AM, Camerlenghi A, Liu CS (eds) World atlas of submarine gas hydrates in continental margins. Springer, Cham, pp 359–371. https://doi.org/10.1007/978-3-030-81186-0_31

Paull CK, Chanton J, Neumann AC, Coston JA, Martens CS, Showers W (1992) Indicators of methane-derived carbonates and chemosynthetic organic carbon deposits: examples from the Florida Escarpment. Palaios 7:361–375. https://doi.org/10.2307/3514822

Paull CK, Ussler W, Borowski WS, Spiess FN (1995) Methane-rich plumes on the Carolina continental rise: associations with gas hydrates. Geology 23(1):89–92. https://doi.org/10.1130/0091-7613(1995)023%3c0089:MRPOTC%3e2.3.CO;2

Paull CK, Ussler W III, Greene HG, Barry J, Keaten R (2005) Bioerosion by chemosynthetic biologic communities on Holocene submarine slide scars. Geo-Mar Lett 25:11–19. https://doi.org/10.1007/s00367-004-0184-z

Paull CK, Caress DW, Thomas H, Lundsten E, Anderson K, Gwiazda R, Riedel M, McGann M, Herguera JC (2015) Seafloor geomorphic manifestations of gas venting and shallow subbottom gas hydrate occurrences. Geosphere 11:491–513. https://doi.org/10.1130/GES01012.1

Roberts J, Wheeler A, Freiwald A, Cairns S (2009) Cold water corals: the biology and geology of deep-sea coral habitats. Cambridge University Press, Cambridge, pp 1–350

Römer M, Sahling H, Pape T, Bohrmann G, Spieß V (2012) Quantification of gas bubble emissions from submarine hydrocarbon seeps at the Makran continental margin (offshore Pakistan). J Geophys Res Oceans 117:C10. https://doi.org/10.1029/2011JC007424

Rubin-Blum M, Antony CP, Borowski C, Sayavedra L, Pape T, Sahling H, Bohrmann G, Kleiner M, Redmond MC, Valentine DL,

Dubilier N (2017) Short-chain alkanes fuel mussel and sponge *Cycloclasticus* symbionts from deep-sea gas and oil seeps. Nat Microbiol 2:17093. https://doi.org/10.1038/nmicrobiol.2017.93

Sahling H, Rickert D, Lee RW, Linke P, Suess E (2002) Macrofaunal community structure and sulfide flux at gas hydrate deposits from the Cascadia convergent margin, NE Pacific. Mar Ecol Prog Ser 231:121–138. https://doi.org/10.3354/meps231121

Sahling H, Bohrmann G, Spiess V, Bialas J, Breitzke M, Ivanov M, Kasten S, Krastel S, Schneider R (2008a) Pockmarks in the Northern Congo Fan area, SW Africa: complex seafloor features shaped by fluid flow. Mar Geol 249:206–225. https://doi.org/10.1016/j.margeo.2007.11.010

Sahling H, Masson DG, Ranero CR, Hühnerbach V, Weinrebe W, Klaucke I, Bürk D, Brückmann W, Suess E (2008b) Fluid seepage at the continental margin offshore Costa Rica and southern Nicaragua. Geochem Geophys Geosyst. https://doi.org/10.1029/2008GC001978

Sato H, Hayashi K-i, Ogawa Y, Kawamura K (2012) Geochemistry of deep sea sediments at cold seep sites in the Nankai Trough: insights into the effect of anaerobic oxidation of methane. Mar Geol 323–325:47–55. https://doi.org/10.1016/j.margeo.2012.07.013

Schnürle P, Liu C-S, Lin AT, Lin S (2011) Structural controls on the formation of BSR over a diapiric anticline from a dense MCS survey offshore southwestern Taiwan. Mar Pet Geol 28:1932–1942. https://doi.org/10.1016/j.marpetgeo.2010.12.004

Scholl DW, von Huene R (2007) Crustal recycling at modern subduction zones applied to the past—issues of growth and preservation of continental basement crust, mantle geochemistry, and supercontinent reconstruction. Geol Soc Am Mem 200:9–32

Sibuet M, Olu K (1998) Biogeography, biodiversity and fluid dependence of deep-sea cold-seep communities at active and passive margins. Deep Sea Res Part II 45:517–567. https://doi.org/10.1016/S0967-0645(97)00074-X

Skarke A, Ruppel C, Kodis M, Brothers D, Lobecker E (2014) Widespread methane leakage from the sea floor on the northern US Atlantic margin. Nat Geosci 7:657–661. https://doi.org/10.1038/ngeo2232

Sloan ED Jr, Koh CA (2007) Clathrate hydrates of natural gases. CRC Press

Suess E (2014) Marine cold seeps and their manifestations: geological control, biogeochemical criteria and environmental conditions. Int J Earth Sci 103:1889–1916. https://doi.org/10.1007/s00531-014-1010-0

Suess E, Carson B, Ritger SD, Moore JC, Jones ML, Kulm LD, Cochrane GR (1985) Biological communities at vent sites along the subduction zone off Oregon. Bull Biol Soc Wash 6:475–484

Suess E, Bohrmann G, Von Huene R, Linke P, Wallmann K, Lammers S, Sahling H, Winckler G, Lutz RA, Orange D (1998) Fluid venting in the eastern Aleutian subduction zone. J Geophys Res Solid Earth 103:2597–2614. https://doi.org/10.1029/97JB02131

Teichert BMA, Bohrmann G, Suess E (2005) Chemoherms on hydrate ridge—unique microbially-mediated carbonate build-ups growing into the water column. Palaeogeogr Palaeoclimatol Palaeoecol 227:67–85. https://doi.org/10.1016/j.palaeo.2005.04.029

Tong H, Feng D, Cheng H, Yang S, Wang H, Min AG, Edwards RL, Chen Z, Chen D (2013) Authigenic carbonates from seeps on the northern continental slope of the South China Sea: new insights into fluid sources and geochronology. Mar Pet Geol 43:260–271. https://doi.org/10.1016/j.marpetgeo.2013.01.011

Torres ME, Bohrmann G, Suess E (1996) Authigenic barites and fluxes of barium associated with fluid seeps in the Peru subduction zone. Earth Planet Sci Lett 144:469–481. https://doi.org/10.1016/S0012-821X(96)00163-X

Ustaszewski K, Wu Y-M, Suppe J, Huang H-H, Chang C-H, Carena S (2012) Crust–mantle boundaries in the Taiwan-Luzon arc-continent collision system determined from local earthquake tomography and 1D models: implications for the mode of subduction polarity reversal. Tectonophysics 578:31–49. https://doi.org/10.1016/j.tecto.2011.12.029

Wang X, Guan H, Qiu J-W, Xu T, Peckmann J, Chen D, Feng D (2022) Macro-ecology of cold seeps in the South China Sea. Geosyst Geoenviron 1:100081. https://doi.org/10.1016/j.geogeo.2022.100081

Wei J, Li J, Wu T, Zhang W, Li J, Wang J, Tao J, Chen Z, Wu Z, Chen W (2020) Geologically controlled intermittent gas eruption and its impact on bottom water temperature and chemosynthetic communities—a case study in the "HaiMa" cold seeps, South China Sea. Geol J 55:6066–6078. https://doi.org/10.1002/gj.3780

Yu H-S, Chang J-F (2002) The Penghu submarine canyon off southwestern Taiwan: morphology and origin. TAO Terr Atmos Ocean Sci 13:547–562